Numerical Study of Three-Dimensional Compressible Flow Structure Within an S-Duct for Aircraft Engine Inlet

Soo-Yong Cho*
Department of Aerospace and Mechanical Engineering
Gyeongsang National University, Chinju, Korea 660-701

Byung-Kyu Park**
Division of Thermal-fluid and Environmental Engineering Research
Korea Institute Machinery and Materials, Taejeon, Korea 305-343

Abstract

Three-dimensional compressible turbulent flow fields within the passage of a diffusing S-duct have been simulated by solving the Navier-Stokes equations with SIMPLE scheme. The average inlet Mach number is 0.6 and the Reynolds number based on the inlet diameter is 1.76×10^6. The extended $k-\varepsilon$ turbulence model is applied to modeling the Reynolds stresses. Computed results of the flow in a circular diffusing S-duct provide an understanding of the flow structure within a typical engine inlet system. These are compared with experimental wall static-pressure, total-pressure fields, and secondary velocity profiles. Additionally, boundary layer thickness, skin friction values, and streamlines in the symmetric plane are presented. The computed results depict the interaction between the low energy flow by the flow separation and the high energy flow by the reversed duct curvature. The computed results obtained using the extended $k-\varepsilon$ turbulence model

Key Word : Engine Inlet Duct, Compressible Flow, CFD, Three-Dimensional Internal Flow, S-Shaped Duct

Introduction

The subsonic duct is a feature of the air intake propulsion system for modern aircraft whether the speed of the aircraft is subsonic or supersonic. The intention of duct design is to produce high pressure recovery in order to maintain high thrust levels, and low flow distortion consistent with stable engine operation. It is common to design ducts to be as short as possible because of size and weight restrictions. Usually, diffusing ducts are employed in the air intake propulsion system of the aircraft in order to decelerate the flow and achieve high pressure recovery at the engine compressor.

S-shaped duct produces complex cross-flow patterns and nonuniform velocity profiles at the exit because of its curvature and centerline offset. These deteriorate the performance of the engine inlet system. The nonuniform flow at the exit results from the expulsion of low velocity fluid by a pair of counter-rotating vortices, which are produced near the inflection point of the duct and stretched toward the exit.

Vakili *et al.*(1987) conducted experiments on a diffusing 30°-30° S-duct with a circular cross-section. Experimental results showed that a pair of counter-rotating vortices which were created by the flow separation caused the flow distortion at the exit of S-duct. Jenkins and Loeffler(1992)

* Assistant Professor
** Senior Researcher

tested on a more compact diffusing S-duct than that tested by Vakili *et al.*(1987). Wellborn *et al.*(1992) conducted experiments on a diffusing S-duct with inlet Mach number as 0.6. Their results also showed that the flow at the exit was strongly affected by a pair of counter-rotating vortices.

Early numerical investigation on a curved pipe is shown in Rowe(1970). Levy *et al.*(1980) conducted computations in a constant-area S-shaped duct using parabolized Navier-Stokes equations with an algebraic turbulence model. The inflow Mach number was 0.2. More detailed results of total-pressure contours and secondary velocity profiles were obtained by Towne and Anderson(1981). Smith *et al.*(1992) conducted a numerical study in a diffusing 30°-30° S-duct using the full Navier-Stokes(FNS) equations with a standard k-ε turbulence model. Their computational results showed that the flow separation region could not be predicted correctly. Cho and Greber(1995) numerically solved the same problems using the FNS equations with a modified algebraic turbulence model. Computed results showed that even modified algebraic turbulence model could not adequately account for strong secondary flows with flow separation. Thus, it can be concluded that an improved numerical analysis method with an advanced turbulence model is necessary to predict correctly the complex flow structure within S-duct.

In this study, computational analysis for the flow fields within S-duct is conducted with the extended k-ε turbulence model. Several aspects of the flow phenomena are examined. Velocity vectors are shown to illustrate the development of secondary velocities in a curved duct. Calculated and measured total- pressure contours are also compared to figure out the underlying physics of the development of secondary flows. A detailed lift-off vortices by the three-dimensional flow separation generated on the duct surface are presented.

Numerical Method

Governing Equations and Turbulence Model

Governing equations employed to describe three-dimensional compressible and turbulent flow fields can be expressed as curvilinear transformed and multi-component conservation equations.

$$\frac{1}{J}\frac{\partial}{\partial t}(\rho\psi)=\frac{1}{J}\frac{\partial}{\partial \xi_i}[-\rho G^i\psi+\Gamma_\psi B^i{}_j(\frac{\partial \psi}{\partial \xi_i})]+S_\psi \tag{1}$$

where $\psi = (1, u, v, w, h, k, \varepsilon)^T$ and each equation represents the continuity, momentum, energy, turbulence kinetic and turbulence dissipation rate equations, respectively. J is the Jacobian of coordinate transformation. $B^i{}_j$ and G^i represent product of the cofactor of J and contravariant velocities, respectively.

$$G^i = u_j\frac{\partial \xi_i}{\partial x_j} \tag{2}$$

$$B^i{}_j = \frac{1}{J}\frac{\partial \xi_i}{\partial x_k}\frac{\partial \xi_j}{\partial x_k} \tag{3}$$

$\Gamma_\psi = (1, \mu+\mu_t, \mu+\mu_t, \mu+\mu_t, k+(\mu_t/Pr_t), \mu_t/\sigma_k, \mu_t/\sigma_\varepsilon)^T$ and the eddy viscosity(μ_t) is obtained by the turbulent kinetic energy(k) and to the rate of its dissipation(ε). Source terms (S_ψ) in Eq.(1) are given in Eq.(5).

$$\mu_t = \rho C_\mu \frac{k^2}{\varepsilon} \tag{4}$$

$$S_\phi = \begin{pmatrix} 0 \\ -P,_x + \nabla \cdot [(\mu_{ef})(u_j,_x)] + \Xi_x \\ -P,_y + \nabla \cdot [(\mu_{ef})(u_j,_y)] + \Xi_y \\ -P,_z + \nabla \cdot [(\mu_{ef})(u_j,_z)] + \Xi_z \\ \frac{DP}{Dt} + \Phi \\ \Theta - \rho\varepsilon \\ C_1 \frac{\varepsilon}{k}\Theta - C_2 \frac{\rho\varepsilon^2}{k} + C_3 \frac{\Theta^2}{\rho k} \end{pmatrix} \tag{5}$$

where Θ represents the turbulent kinetic energy production rate and Φ in the energy equation means energy dissipation function. μ_{ef} is $\mu + \mu_t$ and Ξ_x, Ξ_y and Ξ_z in Eq.(5) are x, y and z component, respectively.

$$\Xi_x = -\frac{2}{3}(\mu_{ef})(\nabla \cdot u_j),_x . \tag{6}$$

In this study, the extended k-ε turbulence model suggested by Chen and Kim(1987) is applied. The difference between the standard and extended k-ε turbulence models is the turbulence dissipation rate equation. The extended k-ε turbulence model includes an extra irrotational strain on the dissipation rate equation, which is a term with coefficient C_3 shown in the last row in Eq.(5). Chen *et al.*(1990) showed that this term allows the dissipation rate to respond to the mean strain more effectively than it does in the standard k-ε turbulence model. Values of modeling constants are as follows;

$$\sigma_k = 0.75,\ \sigma_\varepsilon = 1.15,\ C_1 = 1.15,\ C_2 = 1.90,\ C_\mu = 0.09,\ C_3 = 0.25,\ \mathrm{Pr}_t = 0.9 \tag{7}$$

Numerical Scheme

The governing equations which are transformed by the generalized coordinate are differentiated on the control volume. To achieve accuracy and stability on the convective terms, a second-order central differencing scheme plus adaptive second-order and fourth-order dissipation terms are used to model the convective term. The viscous and source terms of the governing equations are differentiated by the second-order central difference scheme. A first-order upwind scheme is employed for all scalar transport equations. Pressure fields are calculated by the pressure correction equation derived from the continuity equation. A pressure based predictor and multi-corrector solution procedure is applied to ensure velocity-pressure coupling at the end of each time marching step. A time-centered Crank-Nicholson time marching scheme is adopted for the unsteady term and an iterative ADI method is used to solve the discretized algebraic equations.

The mass flow change between the inlet and exit was within 1 percent in all calculations. The residuals for these numerical solutions were reduced to 10^{-4}. The number of iterations required to obtain the converged solutions was approximately 30,000.

Geometry

The geometry of a diffusing S-duct considered in this study is shown in Fig. 1. The duct centerline is defined by two circular arcs with identical radii of curvature, which are 5 times the inlet duct diameter, and subtended angle $\theta_{max}/2=30^\circ$. Both arcs lie within the xy-plane as shown in Fig. 1. The coordinates (x_{cl}, y_{cl}, z_{cl}) of the duct centerline are given by Eqs. (8) and (9):

For $0 \leq \theta \leq \theta_{max}/2$

$$\begin{aligned} x_{cl} &= R \sin \theta \\ y_{cl} &= R \cos \theta - R \\ z_{cl} &= 0 \end{aligned} \tag{8}$$

For $\theta_{max}/2 \leq \theta \leq \theta_{max}$

$$\begin{aligned} x_{cl} &= 2R \sin\left(\frac{\theta_{max}}{2}\right) - R \sin\left(\theta_{max} - \theta\right) \\ y_{cl} &= 2R \cos\left(\frac{\theta_{max}}{2}\right) - R - R \cos\left(\theta_{max} - \theta\right) \\ z_{cl} &= 0 \end{aligned} \tag{9}$$

The cross-sectional shape of the duct perpendicular to the centerline is circular. The diameter of the cross-section varies with the arc angle θ and is given by Eq. (10).

$$\frac{D}{D_i} = 1 + 3\left(\frac{D_e}{D_i} - 1\right)\left(\frac{\theta}{\theta_{max}}\right)^2 - 2\left(\frac{D_e}{D_i} - 1\right)\left(\frac{\theta}{\theta_{max}}\right)^3 \tag{10}$$

where D_i and D_e are the diameter at the inlet and outlet of S-duct, respectively. The area ratio of the duct exit to inlet is 1.51. The offset of the duct resulting from the centerline curvature is $1.34D_i$. The length of the duct measured along the centerline is $5.24D_i$. A straight pipe, which is $4.6D_i$ long, is installed upstream of the S-duct to provide the desired boundary layer thickness at the inlet of S-duct. In order to minimize any downstream effect, a $9D_e$ straight section of pipe is attached at the exit of duct. The average inlet Mach number is 0.6 and the Reynolds number based on the duct diameter(D_i) is 1.76×10^6.

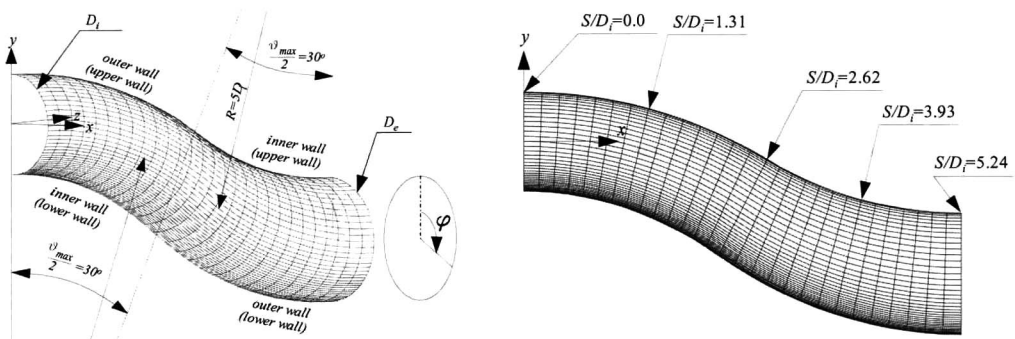

(a) Half section of S-duct

(b) Side view for measurement stations

Fig. 1 Geometry definition for the diffusing S-duct

Grid and Boundary Conditions

An O-grid is adopted because it conforms well to the boundaries of the circular duct. The O-grid consists of 30 radial points, 42 circumferential points in the half of duct cross-sectional area, and 69 streamwise nodal points. A finer grid is used in the region of flow separation. Exponential stretching is used to obtain a fine mesh near the wall. Meshes in the upstream and downstream regions of straight ducts are also extended using the exponential stretching. The mesh size adjacent to the duct surface is almost 1.25×10^{-4} times the duct inlet diameter. The two grid points nearest

the wall are at value of y^+ of about 2.6 and 5.7 at the reference station (S/D_i=-1.5).

An adiabatic wall condition is imposed by setting the normal derivative of temperature equal to zero. Constant stagnation pressure and temperature are specified at the entry plane, deriving from experimental values obtained at the reference station. Axial velocities at the inlet are calculated from the characteristic equation derived from the one-dimensional Euler equation because the flow speed in the whole computational domain is subsonic. Static-pressure is specified at the exit plane and linear extrapolation is adopted for evaluating the exit velocities. A pole boundary condition was used for the center of the O-grid by averaging the surrounding flow properties.

Results and Discussion

Fig. 2 shows surface static-pressure distributions at φ =10°, 90° and 170° which are compared with two experimental data of Vakili *et al.*(1987) and Wellborn *et al.*(1992), and computed results obtained by Smith *et al.*(1992) using the standard $k-\varepsilon$ turbulence model. Wellborn *et al.*(1992) used a similar duct but larger than that used by Vakili *et al.*(1987); therefore, the Reynolds number on the experiment conducted by Wellborn *et al.*(1992) was 47% higher than that by Vakili *et al.*(1987) and this computation. The computed surface static-pressure distributions show good agreement with the experimental data except in the flow separation region.

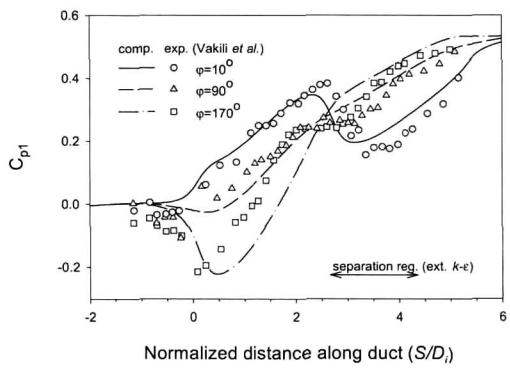

(a) $C_{p1}=(P_{local}-P_{center})/q_{ref}$

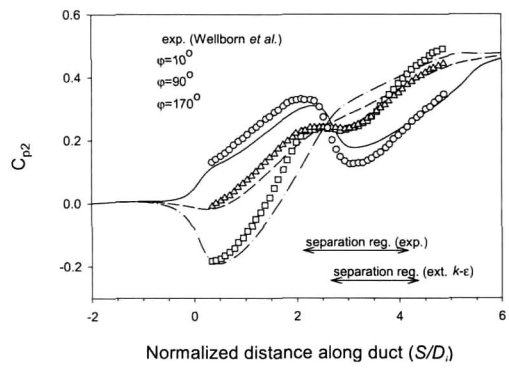

(b) $C_{p2}=(P_{local}-P_{wall})/q_{ref}$

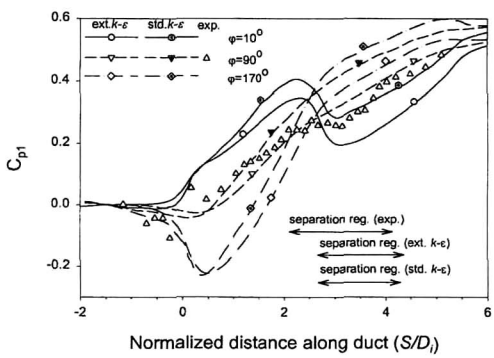

(c) C_{p1} with standard $k-\varepsilon$ turbulence model

Fig. 2 Axial surface static-pressure coefficient compared with experimental results (Vakili *et al.*(1987) and Wellborn *et al.*(1992)) and computed result (Smith *et al.*(1992))

Experimental flow separation region was determined by surface oil flow visualization. Computed flow separation region is determined by examining the velocity at the first grid point off the duct surface along $\varphi=180^{\circ}$. In the separation region, the predicted surface static-pressure are higher than the measured values. Both experimental data show constant values of static-pressure at $\varphi=90^{\circ}$ and 170° in the region of $2\leq S/D_i\leq 3$; the computational result shows that the surface static-pressure distributions are bended down at $S/D_i=3.0$. Computed flow separation length is $1.66D_i$, which is a little shorter than the experimental value of $2.11D_i$. The predicted flow separation region ($2.64\leq S/D_i\leq 4.30$) occurs farther downstream than that observed experimentally ($2.02\leq S/D_i\leq 4.13$). This indicates that the turbulence model does not correctly account for the three-dimensional separation flow with very strong secondary flow.

Fig. 2(c) shows that the computed results obtained by the standard $k-\varepsilon$ turbulence model show much deviation in the low momentum fluid region, *i.e.* in the second half bend of S-duct, than those by the extended $k-\varepsilon$ turbulence model. The experimental surface static-pressure coefficients at $\varphi=90^{\circ}$ are plotted as representative experimental data in Fig. 2(c). Even though the computed results obtained by the extended $k-\varepsilon$ turbulence model show some deviations on the surface static-pressure coefficient in the flow separation region, the extended $k-\varepsilon$ turbulence model follows the experimental data in the flow separation region and downstream region more closely than the standard $k-\varepsilon$ turbulence model.

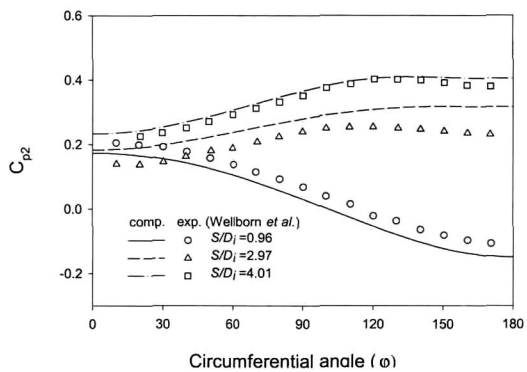

Fig. 3 Circumferential surface static-pressure coefficients

Fig. 3 shows the surface static-pressure distributions along the circumferential direction at three different streamwise locations S/D_i=0.96, 2.97 and 4.01. Computed results at S/D_i=4.01 agree quite well with the experimental data measured by Wellborn *et al.*(1992). The measured data points are located downstream of the flow separation region except the lower wall of the second half bend. The computed surface static-pressure coefficients at S/D_i=0.96 are lower than the experimental data even though it is located upstream of the flow separation region. The reason is that the boundary layer thickness on the computation is thinner than that on the experiment at the inlet of S-duct. Although a straight duct of $4.6D_i$ long is installed to obtain the desired boundary layer thickness at the inlet of S-duct, the length of straight duct is a little short. Steep velocity profiles normal to the surface are obtained on the computation within the boundary layer at S/D_i=0.96. The computed values of surface static-pressure at S/D_i=2.97, which is located within the flow separation region, are higher than the experimental data. This over-prediction indicates that the blockage resulting from the boundary layer separation, as previously mentioned, is under-predicted by the turbulence model.

Secondary velocity profiles at four stations along the duct are shown in Fig. 4. They are compared with the experimental data obtained by Vakili *et al.*(1987). Since the flow is symmetric with respect

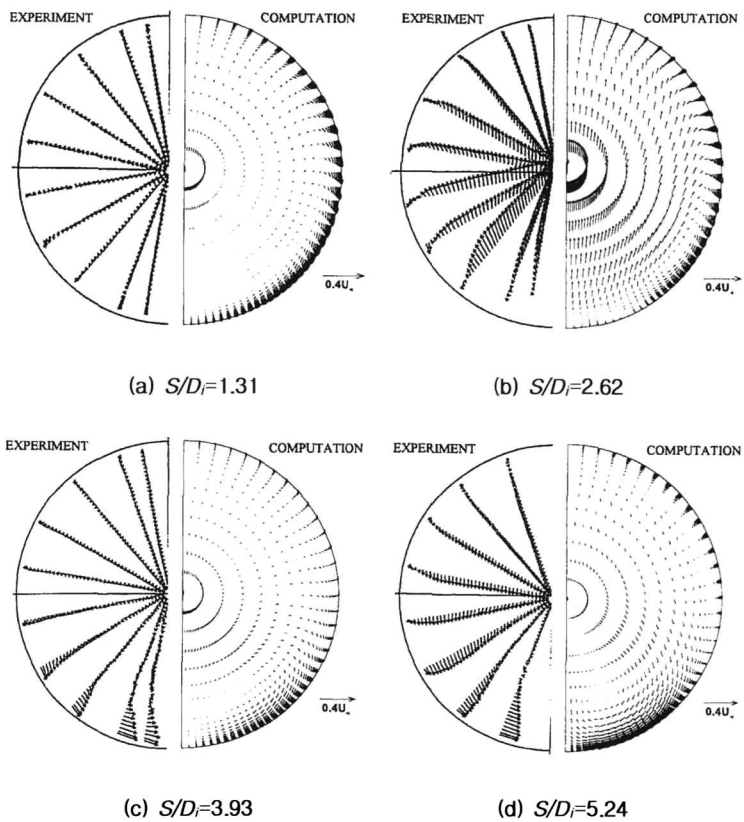

Fig. 4 Secondary velocity profiles along the streamwise direction

to a vertical plane passing through the centerline, the computed and experimental results are plotted at each half of cross-section. The computational results are in good agreement with the experimental data except in the flow separation region. The secondary velocity profiles in the S-duct clearly depict the qualitative picture of the secondary flow pattern in a curved duct. The development of secondary flow in a curved duct is that an inviscid core fluid moves toward the outer wall of the duct due to the centrifugal force, and the low speed fluid in the boundary layer migrates circumferentially from the outer wall to the inner wall in order to satisfy the constant mass flux. This phenomenon is shown in the first half bend of S-duct, and it results in the accumulation of low energy flow near the inner wall on the first half bend of S-duct. The low static-pressure is developed in the same region as shown in Fig. 3. The adverse pressure gradient is induced on the second half bend of S-duct due to the increase of the duct area. The pressure gradient causes a thick boundary and deflection of the streamwise flow direction as shown in Fig. 4(b).

Total-pressure contours at four stations along the flow direction are shown in Fig. 5, and experimental data was obtained by Vakili *et al.*(1987). The accumulation of low energy flow in the lower wall is shown in these figures. The above mentioned secondary flow pattern contributes to the formation of a pair of counter-rotating vortices by the three- dimensional flow separation. Tobak and Peake(1982) showed the topographical structure of three-dimensional flow separation. The counter-rotating vortices formed by the vortex lift-off stretch to the exit of S-duct by the streamwise velocity, and move away from the wall to the center of the duct. In the region between two counter-rotating vortices, the secondary velocities induced by the vortices push up the low energy flow toward the center of the duct. Additionally, the secondary velocities induced by the vortices push down the high

energy flow in the region between the vortices and the duct side wall. This mechanism makes the convex shape of the inviscid core flow region. This results in the nonuniform flow at the exit of S-duct.

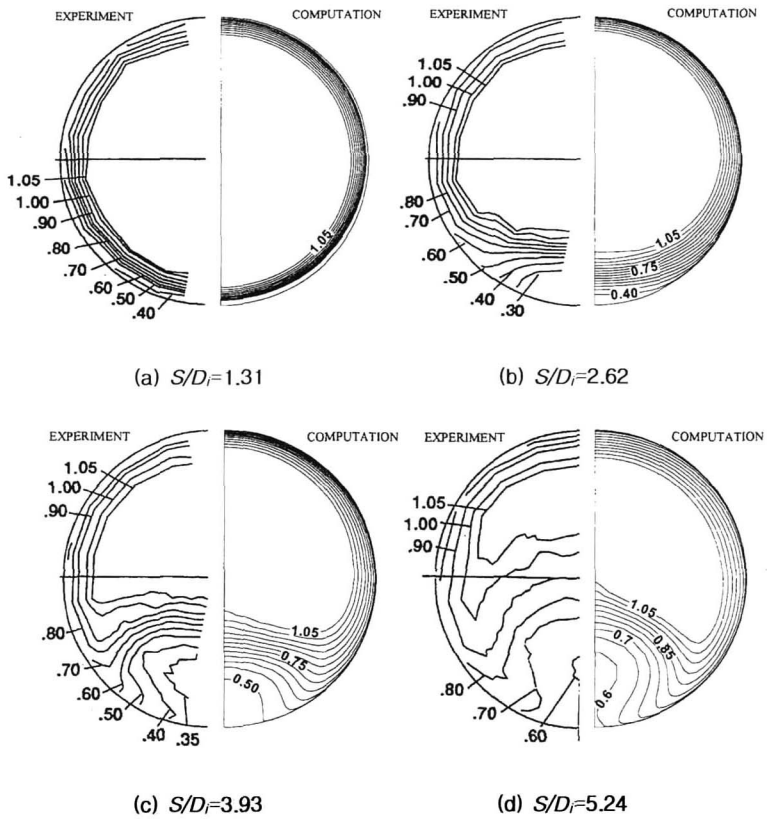

(a) S/D_i=1.31 (b) S/D_i=2.62

(c) S/D_i=3.93 (d) S/D_i=5.24

Fig. 5 Total-pressure coefficient contours along the streamwise direction

The shape of the total-pressure contours in the cross plane depends on the strength of the counter-rotating vortices and the core location of the vortices in the same plane. They depend on the original locations of the counter-rotating vortices in the duct. The computed three-dimensional flow separation region occurred farther downstream than observed in two experiments. This causes the discrepancy between the computational and experimental total-pressure contours at S/D_i=5.24. The computed total-pressure contours at S/D_i=5.24 show that the change rate of the streamwise velocity deficit(U_∞-U) at the region of the counter-rotating vortices is steeper than that observed experimentally. This steep change of streamwise velocity deficit makes the inviscid core region larger to conserve mass flux along the streamwise direction.

Computed streamlines near the wall in the region of three-dimensional flow separation are compared with the experimental surface flow visualization obtained by Wellborn *et al.*(1992) as shown in Fig. 6(b). The flow in Fig. 6 comes from left to right and the view is looking at the center of circular arc in the second half bend of S-duct *i.e.* the center of the centerline given in Eq. (8). The pair of spiral nodes in the computed surface streamlines indicate an origin of vortex lift-off generated by the three-dimensional flow separation. The lift-off vortices form the counter-rotating vortex moving down to the duct exit and lift up the low energy flow to the duct center in the second half bend of S-duct. These cause the large flow angle relative to the x-axis in the circumferential region of

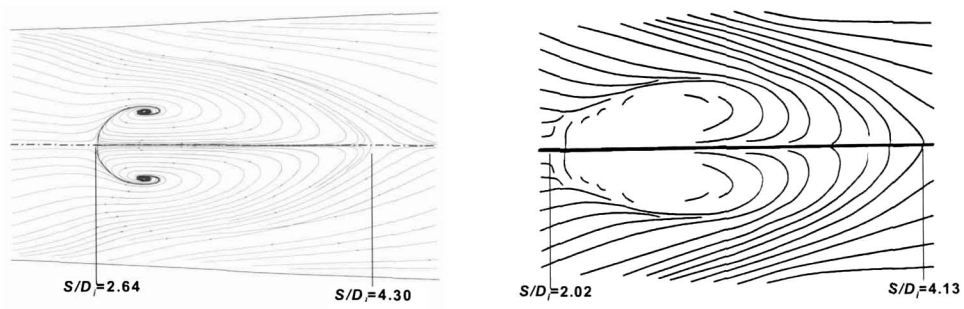

(a) Computation (b) Experiment

Fig. 6 Streamlines near the S-duct surface compared with the experimental result by Wellborn *et al.*(1992)

flow separation. This feature is the typical three-dimensional flow separation phenomena. The computed result shows that the flow separation is developed at farther downstream than experimental result, and the computed flow separation region(S/D_i=1.66) is more narrow than the experimental result(S/D_i=2.11). The computed result obtained by Smith *et al.*(1992) using the standard $k-\varepsilon$ turbulence model showed that the flow separation was started at S/D_i=2.64 which is the same as this computation as shown in Fig. 2(c), but the flow separation region was S/D_i=1.59, which was shorter than the computed result obtained using the extended $k-\varepsilon$ turbulence model. The shape of vortex formation near the wall agrees well with the experimental result qualitatively.

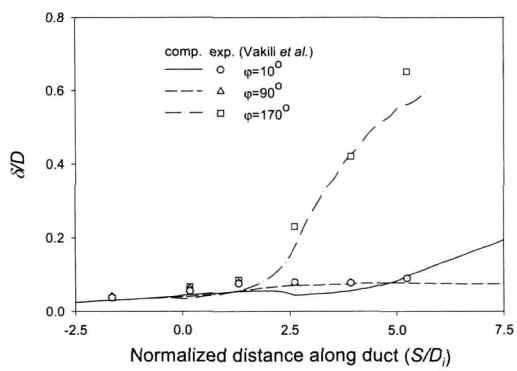

Fig. 7 Bounday layer growth versus normalized distance along duct centerline

Variations of boundary layer thickness at φ=10°, 90° and 170° along the duct are shown in Fig. 7. The boundary layer thickness is defined as the normal distance from the wall where the total-pressure coefficient is 1.0. The predicted results are compared with experimental results obtained by Vakili *et al.*(1992). Computational results and experimental data are in reasonable agreement. The rapid boundary layer growth at φ=170° is caused by the flow separation. In the transition region (S/D_i=0) from the straight duct into the first half bend of S-duct, the computed results show that boundary layer thickness at φ=170° is less than that at φ=10°. The streamwise velocity near the lower wall in the transition region is faster than that near the upper wall due to the effect of curved geometry. It was well depicted in the axial static-pressure coefficient plot as shown in Fig. 2. The experimental data do not clearly show the effect of this flow mechanism. As shown in the secondary

flow pattern of Fig. 4, the high energy flow migrates toward the outer wall in the first half bend of S-duct; therefore, the increasing rate of boundary layer thickness at $\varphi=10^{\circ}$ along the duct is less than that at $\varphi=90^{\circ}$ and 170°. At downstream of the flow separation *i.e.* in the straight duct connected at the S-duct exit, the computational result shows that the boundary layer thickness at $\varphi=90^{\circ}$ is less than that at $\varphi=10^{\circ}$. The reason is that the strong secondary velocities induced by the counter-rotating vortices push the high energy flow toward the wall. The high energy flow effect by the secondary velocities at $\varphi=90^{\circ}$ is bigger than that at $\varphi=10^{\circ}$ because the cores of counter-rotating vortices moving downstream are located between the duct center and the lower wall.

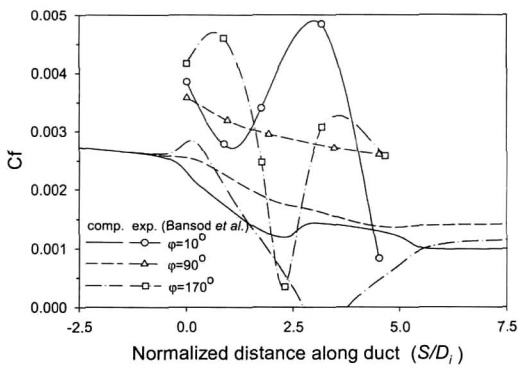

Fig. 8 Coefficient of skin friction versus normalized distance along duct centerline

Skin friction coefficients are plotted along the streamwise direction for $\varphi=10^{\circ}$, 90° and 170° in Fig. 8. The local skin friction coefficient is computed wall shear stress divided by the reference dynamic-pressure. Note that experimentally determined skin friction values are not available on a diffusing S-duct, however, the experimental data obtained by Bansod and Bradshaw(1972) for low speed flow in a non-diffusing S-duct provides an appropriate check for the trend observed in the computed results. The non-diffusing S-duct used in their experiment was assembled with a straight section between two bended tubes having different radii of curvature. The centerline radius of curvature at the first half bend was 2.25 times the tube diameter and the second half bend having the centerline radius of curvature R/D_i=3.5 followed the straight tube 0.5 times the tube diameter long. Trends of the computed skin friction coefficients are similar to those of the experimental data. The values of skin friction coefficient in the non-diffusing S-duct experiment are bigger than those in the computed results because the reference dynamic-pressure in the diffusing S-duct is 18.7 times bigger than that in the experiment. The skin friction coefficients are decreased along downstream due to the decrease of shear stress by the expansion of duct area. The skin friction coefficients for $\varphi=170^{\circ}$ is cut off in the region of the flow separation because the direction of shear stress is reversed due to the back flow as shown in Fig. 6.

Fig. 9 shows streamlines in the symmetry plane of the S-duct. The experimental result was obtained by placing a thin metal plate in the symmetry plane of the S-duct. Even though there is no cross-flow in this symmetry plane, the presence of thin plate in the symmetry plane introduces shear layer development and blockage. Additionally, rolled-up flows in the symmetry plane get stronger by the presence of thin plate. The experimental result obtained by Wellborn *et al.*(1992) shows strong rolled up flows after the region of flow separation as shown in Fig. 9(c), but computed results show that the height of rolled up flows by the lift-off vortex is less than that in the experiment. This difference between the experimental and computed result comes up by the presence of thin plate. The computed result is consistent because traverse velocities toward y-direction does not influence to the center of the duct in the symmetry plane as shown in the experimental secondary velocity profiles at the S-duct exit of Fig. 4(d). However, comparison with the experimental result agrees well qualitatively.

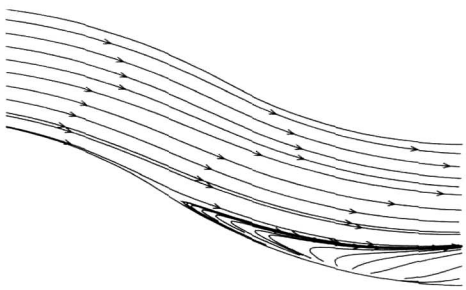

(a) Extended $k-\varepsilon$ turblence model

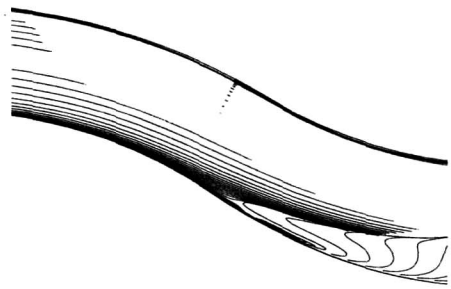

(b) Modified algebraic turbulence model by Cho and Greber(1995)

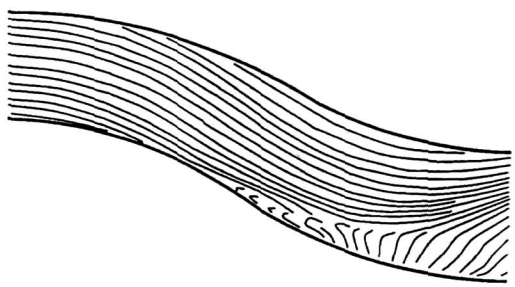

(c) Experimental result by Wellborn *et al.*(1992)

Fig. 9 Streamline in the symmetry plane of the S-duct

The computed streamlines obtained by the extended $k-\varepsilon$ turbulence model show an improved result compared with those obtained by Cho and Greber(1995), which used the modified algebraic turbulence model. In the computed result obtained using the modified algebraic turbulence model, back flows in the flow separation region are generated off the wall surface as shown in Fig. 9(b). The reason was that the incorrect turbulent length scales were chosen in the computation for the three-dimensional flow separation region. Eddy viscosity turbulence models are usually derived and validated for two-dimensional boundary layer flows. Further, the eddy viscosity coefficient determined by these models depends on the local flow profiles along the normal direction from the wall. However, for the flows over more complex configurations, where the boundary layers and wakes may interact or flow separation may occur, the major difficulty encountered in applying the eddy viscosity turbulence model in that of properly evaluating the length scale. Even Cho and Greber(1995) modified the Baldwin-Lomax(1978) turbulence model in computing the three-dimensional separated flow by choosing the first maximum value of $F(y)$ away from the wall and evaluating the cut-off distance in every cross plane to insure that y_{max} was less than the boundary layer thickness, the chosen length scale was smaller than the physical length scale. When the extended $k-\varepsilon$ turbulence model is applied, back flows in the three-dimensional flow separation region generate on the wall surface as shown in Fig. 9(a). That is physically reasonable and agrees well with the experimental result.

Conclusions

In the current computations, computed results depict well flow structures in the diffusing S-duct. The extended $k-\varepsilon$ turbulence model shows good capability to predict the flow fields of three-dimensional flow separation with strong secondary flows. Computed total-pressure contours are generally in good

agreement with experimental data, and the flow distortion at the exit of S-duct is predicted with the development of the low energy fluid by the three-dimensional flow separation. The secondary velocity vector profiles are in qualitative agreement with the test data. Two counter-rotating vortices at the exit of S-duct are developed by the vortex lift-off from the lower wall. Predicted surface static-pressure coefficients are in reasonable agreement with measurements except flow separation region. Even though surface static-pressure coefficients in the flow separation region are predicted higher than those observed experimentally, the predicted surface static-pressure coefficients downstream of the flow separation follow well the experimental data. The computed results obtained with the extended $k-\varepsilon$ turbulence model follow the experimental data more closely than the computed results obtained with the modified algebraic turbulence model or the standard $k-\varepsilon$ turbulence model. However, the computed results provide inadequate information about the flow structure, such as the flow separation region or vortex strength, in the three-dimensional flow separation region with strong secondary flows even with the extended $k-\varepsilon$ turbulence model. Additional work will be needed to correctly account the turbulent flow imbedded vortices with strong secondary flows, and a higher order upwind numerical scheme should be tested for studying scheme dependence on the computations. Additional comprehensive experimental data should be obtained for validating the computed results.

References

Bansod, P. and Bradshaw, P., 1972, "The Flow in S-shaped Ducts," *the Aeronautical Quarterly,* Vol. 23, pp. 131-140

Baldwin, B. S. and Lomax, H., 1978, "Thin Layer Approximation and Algebraic Model for Separated Turbulent Flows," AIAA-78-257

Chen, Y. S., and Kim, S. W., 1987, "Computation of Turbulent Flows using a Extended k- ε Turbulence Closure Model," NASA CR-179204

Chen, Y. S., Farmer, R. C., Freeman, J.A., 1990, "The Use of Variational Principle in Improving Computational Fluid Dynamics Methodology," NASA contract NAS8-3740

Cho, S. Y. and Greber, I., 1995, "Three Dimensional Compressible Turbulent Flow Computations For a Diffusing S-Duct," NASA-CR-195390

Jenkins, R. C. and Loeffler, A. L., 1992, "Modeling of Subsonic Flow Through a Compact Offset Inlet Diffuser," *AIAA J.,* Vol. 29, pp. 401-408

Levy, R., McDonald, H., Briley, W. R. and Kreskovsky, J. P., 1980, "A Three-Dimensional Turbulent Compressible Subsonic Duct Flow Analysis for Use with Constructed Coordinated Systems," AIAA-80-1398

Rowe, M., 1970, "Measurements and Computations of Flow in Pipe Bends," *J. Fluid Mech.,* Vol. 43, pp. 771-781

Smith, C. F., Bruns, J. E., Harloff, G. J. and DeBonis, J. R., 1992, "Three-Dimensional Compressible Turbulent Computations for a Diffusing S-Duct," NASA-CR-4392

Tobak, M. and Peak, D. J., 1982. "Topology of Three-Dimensional Separation Flow," *Ann. Review Fluid Mech.,* Vol. 14, pp. 61-85

Towne, C. E. and Anderson, B. H., 1981, " Numerical Simulation of Flows in Curved Diffusers with Cross-Sectional Transitioning Using a Three-Dimensional Viscous Analysis," NASA TM81672

Vakili, A. D., Wu, J. M., Bhat, M. K. and Liver, P. A., 1987, "Compressible Flow in a Diffusing S-Duct with Flow Separation," in *Heat Transfer and Fluid Flow in Rotating Machinery* edited by Yang, W.J., Hemisphere publishing Corporation, pp. 201-211

Wellborn, S. R., Reichert, B. A. and Okiishi, T. H., 1992, "An Experimental Investigation of the Flow in a Diffusing S-Duct," AIAA-92-3622